Effects of flow unsteadiness and chemical kinetics on the reaction yield in a T-microreactor

A. Mariotti[a,*], M. Antognoli[a], C. Galletti[a], R. Mauri[a], M.V. Salvetti[a], E. Brunazzi[a]

[a] *Dipartimento di Ingegneria Civile e Industriale, Università di Pisa, Largo Lucio Lazzarino, 2, 56122 Pisa, Italia*

Abstract

Experimental flow visualizations and velocity measurements are used jointly with numerical simulations to investigate the mixing and monitor the reaction progress in the periodic flow regimes occurring in a T-shaped microreactor. We considered the effects of different kinetic constants, with very different characteristic chemical time scales resulting in a wide range of Damköhler numbers.

A remarkable agreement between experiments and simulations is found both in terms of flow pattern and reaction progress. Two different flow regimes are present for increasing Reynolds number. The first is the periodic asymmetric regime, characterized by the shedding of vorticity-blobs along the mixing channel leading to a further increase of the mixing performance compared to the steady engulfment regime. The second regime is the periodic asymmetric one, which is mainly a poor-mixed segregated regime with

*Corresponding author

Email addresses: alessandro.mariotti@for.unipi.it (A. Mariotti), matteo.antognoli@phd.unipi.it (M. Antognoli), chiara.galletti@unipi.it (C. Galletti), roberto.mauri@ing.unipi.it (R. Mauri), mv.salvetti@ing.unipi.it (M.V. Salvetti), elisabetta.brunazzi@unipi.it (E. Brunazzi)

periodic oscillation at the interface between the two reactants. The mixing degree significantly increases in the unsteady asymmetric regime, whereas it predictably drops down in the unsteady symmetric regime. In the periodic asymmetric regime the reaction yield follows the same function of the Damköhler number, describing the residence to chemical time-scale ratio, and of a non-dimensional kinetic constant, taking into account also fluid properties, previously proposed for the steady vortex and engulfment regimes. In the periodic symmetric regime, the reaction yield is found to depend only on the Damköhler number, with the same dependence previously highlighted for the steady segregated regime.
Keywords: T-microreactors, unsteady flow regimes, Reynolds number, mixing degree, reaction yield

1. Introduction

In many engineering applications, batch operations could be replaced by continuous processes taking place within microreactors ensuring a superior control of the operating conditions and allowing a significant process intensification [1–3]. In addition, the complex scale-up of batch units to industrial volumes can be replaced by a simple numbering up, that is the process of multiplying the number of microreactors, which are often assembled in modular systems [4–6]. Another important advantage of microreactors is that the large surface-to-volume ratio, typical of microfluidic devices, allows a much larger heat transport, so that strongly exothermic, potentially dangerous, reactions can be safely dealt with [7, 8]. Indeed, reactions as the direct fluorination of aromatics or the synthesis of trinitroglycerin, can be safely processed in

microreactors even at relatively high temperatures [9].

Despite the above very attractive aspects, the practical adoption of microreactors has been limited so far. This fact is partly due to some major drawbacks to be faced. One of the issues is to efficiently mix the reactants. Indeed, the flow regime is laminar because of the small dimensions; hence mixing is diffusion-controlled and thus quite inefficient. Large attention has been devoted to optimize the geometry as well as the operating conditions of microdevices to break the flow symmetries, promoting the mixing process by splitting and recombination of the flow streams [10–15].

One of the most studied microreactor geometry is the T-junction [16–19]; despite its simplicity, it exhibits a rich and very complex fluid mechanical behavior, depending on the Reynolds number, Re (see reviews in [20, 21]). Indeed, while for small Re the two inlet streams remain separated within the mixing channel (segregated regime), increasing Re results in the appearance of two pairs of counter-rotating vortices (steady symmetric regime) that nevertheless do not allow the two inlet streams to intermingle. Then, at larger Re, the mirror symmetry of the flow fields breaks down, resulting in a central point symmetric engulfment flow (steady asymmetric regime) that strongly intermixes the two incoming streams with a consequent significant increase of the degree of mixing [22, 23]. Upon further increasing Re, the fluid flow becomes unsteady and time-periodic, still exhibiting flow asymmetry (unsteady asymmetric regime) that further boosts mixing. However, a further increase of Re leads to the unexpected behavior that the fluid flow, although remaining time periodic, acquires back the mirror symmetry with two pairs of counter-rotating vortices (unsteady symmetric regime), resulting in a drastic

drop of the degree of mixing. Finally, at even larger Re, the flow becomes chaotic.

Despite the fact that a large body of literature has been devoted to study the effects that changes in the geometry (see, e.g. [24]) or in the operating conditions (see, e.g. [25, 26]) have on mixing, surprisingly little attention has been paid to study their effect on the yield of chemical reactions. However, the real purpose of microreactors is to achieve high reaction yield rather than mixing and in this perspective both mixing and chemical kinetics may play a role. Only recently, in a series of articles [27–29], we have investigated, both numerically and experimentally, the case when the inlet flows of a T-microreactor carry chemical species which, upon mixing, react with each other. Here, in addition to Re, that determines the degree of mixing, we investigate the sensitivity to the reaction rate, and thus to the Damköhler number, Da, expressing the ratio between convection and reaction time scale. First, in [27] and [28], we have considered the case of relatively small Re, corresponding to steady state regimes, finding an explicit dependence of the reaction rate, η, on Da. Finally, in a recent work [29], we have presented preliminary results for reactive flows at larger Re, corresponding to unsteady flow regimes, for a single reaction rate. We showed that, while the reaction yield may increase significantly in the unsteady asymmetric regime, it predictably drops down in the unsteady symmetric regime.

In the present work we want to extend the results of the above investigation, considering the effects of different reaction rates, with different characteristic chemical time scales resulting in a wide range of Da. To this aim, experimental flow visualizations and micro-PIV velocity measurements are used together

with numerical simulations. The synergic use of experiments and simulations indeed allows us to derive general trends of the reaction yield with varying flow dynamics, mixing performance and reaction rate. Finally, the contribution of the different phenomena characterizing the periodic flow dynamics to the mixing performance and reaction yield is evaluated by investigating the time-behavior of mixing and reaction performance.

2. T-reactor and chemicals

The geometry of the T-reactor is shown in Fig. 1a and has been described in previous works [20, 27, 28, 30], and thus only a few details are briefly recalled herein. It consists of two identical inlet channels with $H = 1mm$ square cross section and a mixing channel having $2:1$ aspect ratio, so that its hydraulic diameter is $d = 4H/3$ (in the following, distances will be scaled by d). The length of the inlet channels is $L_i = 30d$, so that at the T-junction we may safely assume that the flow is fully developed. The length of the mixing channel is $L_o = 45d$, so at the exit of the mixing channel all vortical structures are expected to have completed their evolution. The T-reactor is built of three transparent layers made of polymethylmethacrylate (PMMA). Figure 1b shows a picture of the device; the central layer, 1 mm thick, has the T-shaped cut through and is sealed to the top and bottom layers by means of two double-sided adhesive films and screws. The top layer, 3 mm thick, is equipped with connections for inflow and outflow.

The test reaction is the reduction of MB^+ (methylene blue) to the colorless LMB^+ (leucomethylene blue) by means of AsA (ascorbic acid) and catalyzed

by HCl (hydrogen chloride), i.e. [27–29]:

$$\mathrm{MB}^+ + \mathrm{AsA} \xrightarrow{HCl} \mathrm{LMB}^+ + \mathrm{DA} \tag{1}$$

where DA is the dehydroascorbic acid.

Clearly, indicating by square brackets the molar concentrations (in mol/L), we see that the temporal growth rate of [DA] and [LMB^+] must equal to each other and to the temporal reduction rate of [MB^+] and [AsA] while [HCl] remains constant. The kinetics of the above reaction follows a pseudo-first order law in case of an excess of ascorbic acid ([31]), hence we can write:

$$\frac{d[\mathrm{MB}^+]}{dt} = \frac{d[\mathrm{AsA}]}{dt} = -\frac{d[\mathrm{DA}]}{dt} = -\frac{d[\mathrm{LMB}^+]}{dt} = -k_r[\mathrm{MB}^+]; \quad \frac{d[\mathrm{HCl}]}{dt} = 0, \tag{2}$$

where the kinetic constant depends on the HCl concentration as

$$k_r = (k_0 + k_1[\mathrm{HCl}])[\mathrm{AsA}] \tag{3}$$

Here $k_0 = 1$ L mol^{-1} s^{-1} and $k_1 = 5.3$ L^2 mol^{-2} s^{-1}.

The aqueous solution of MB^+ and HCl is fed into one inlet channel of the T-reactor, while the aqueous solution of AsA is fed into the other. Then, following the protocol described in [20], we prepare different mixtures where, by varying [HCl] and [AsA], we obtain two fairly different values of $k_{r,0}$. In particular, the aqueous solutions of MB^+ and HCl are prepared by dissolving methylene blue trihydrate powder (CAS No.7220-79-3, Merck KGaA, Germany) in aqueous solutions of HCl. The concentration of MB^+ is kept fixed and equal to [MB^+] $= 5.31 \times 10^{-5}$ mol/L, while two different concentrations of HCl are considered, namely [HCl] $= 0.1$ and 1 mol/L (CAS No. 7647-01-0) supplied by Merck KGaA (Darmstadt, Germany). Ascorbic

acid solutions are prepared by dissolving L-ascorbic acid (Ultrafine vitamin C powder by Cutetonic Ltd, London, SW17 9SH, UK) in deionized water, to obtain [AsA]= 0.85 and [AsA]= 1.7 mol/L, respectively. The water deionization is granted by two purification steps, viz., a reverse osmosis process followed by ionic exchange filtration. For all these concentrations, the pseudo-first order hypothesis holds as the MB^+ concentration was less than 1% of the HCl and AsA ones. A pseudo-first order kinetic constant $k_{r,0} = 1.30$ is obtained for [AsA]=0.85 mol/L and [HCl]=0.10 mol/L, whereas $k_{r,0} = 10.71$ is obtained for [AsA]=1.7 mol/L and [HCl]=1.00 mol/L. The physical properties depend on the AsA concentration. In particular, the solution with [AsA] = 0.85 mol/L has $\rho = 1.058$ g/cm^3, $\mu = 1.003$ mPa s and $\nu = 1.19$ mm^2/s, whereas the solution with [AsA] = 1.7 mol/L has $\rho = 1.117$ g/cm^3, $\mu = 1.7$ mPa s and $\nu = 1.52$ mm^2/s. Note how the differences in density are rather small and, hence, at the high Reynolds characteristic of the unsteady regimes the effects of stratification are expected to be limited. On the other hand, the reaction rate varies of one order of magnitude and this, in turn, implies a large variation of the Damköhler number.

A KD Scientific Inc. (Holliston, MA 01746 USA) syringe pump Gemini 88, equipped with two Becton Dickson plastic syringes of 60 mL, delivers at the same well-controlled flow rate the aqueous solutions of MB^+ and HCl into one inlet channel of the reactor and the aqueous solutions of AsA into the other inlet. Thus, both streams have equal inlet bulk velocity, U. The pump is stopped after each test and then started again imposing the new flow rate; this procedure is aimed at avoiding any hysteresis phenomena in the mixing and reaction process.

3. Particle Image Velocimetry, flow topology and reaction yield measurements

A planar two-component Dantec Dynamics (Denmark) Particle Image Velocimetry (PIV) is used to gain insight in velocity field and flow structure in different planes normal to the z direction [32, 33]. The PIV set-up (Fig. 1c) is the same as in [28] and it is briefly recalled herein together with the acquisition parameters used for the unsteady regimes. The field of view is imaged by an upright microscope model Nikon (Japan) Eclipse 80i equipped with a magnifying lens of $4\times$ having aperture value equal to $N.A. = 0.13$. The images are collected by using a digital CCD Camera having a rectangular monochrome sensor with a resolution of 1344×1024 pixels, with a high sensitivity in the visible and infrared light spectrum. In front of the camera a $0.7\times$ lens is mounted to collect a region of $2.325d \times 1.77d$ in a single image (the equivalent dimension of a pixel is 2.3 μm), corresponding to the whole T-junction region. The two entering streams are seeded with Molecular Probes Fluospheres by Invitrogen ltd (UK), having a diameter of 1 μm. A microstrobe light source (Dantec Dynamics, Denmark) is used as a volume illumination and the microscope objective's depth-of-field determines the thickness of the measurement volume. The microstrobe is a pulsed light source, having a wavelength of 530 nm. The time between two subsequent pulses are set equal to $\Delta t = 100$ μs for the measurements at $Re = 320$ and $\Delta t = 60$ μs for $Re = 500$, to have an appropriate displacement of particle tracers for obtaining reliable velocity data. According to [34], the thickness of the measurement volume can be estimated equal to $0.125d$; thus up to 9 measurements planes can be distinguished in the T-reactor depth.

For each configuration, a total of 100 image pairs are processed with Dantec adaptive PIV tools using a final interrogation window of 16×16 pixels and overlap of 50%, leading to a spacing equal to $0.028d$ of the velocity vectors in the collection region. To improve the signal-to-noise ratio, during the pre-processing of the images (before the correlation), we first subtract the background from the PIV recorded images to reduce the background noise. Moreover, thanks to adaptive-PIV techniques, the signal-to-noise ratio is improved by balancing the use of results from small interrogation areas (8×8 pixels), which have high spatial resolution and lower signal-to-noise ratio, and increasing the size of the correlation windows (up to 64×64 pixels), which have higher signal-to-noise ratio and reduced spatial resolution. At the end of this adaptative procedure, image pairs are presented in the paper using a final interrogation window of 16×16 pixels. In addition to this, spurious vectors due to insufficient seeding particle density are eliminated. All the experiments were performed in a dark room in order to maintain a constant level of luminosity and to minimize any reflection and shadow.

The flow topology and the progress of the color-fading reaction at the confluence region and along the mixing channel, were evaluated by using the same setup as in [29]. For these measurements, a high-speed camera Optomotive Velociraptor HS (Slovenia) with an up-mounted 0.7x lens was used. Image were collected with a resolution of 780×1504 pixels and an acquisition frequency of 450 frames/s. The image exposure time is significantly shorter than the one related to the frame rate, i.e., $\delta t = 10^{-6}$ s. Each image collects a region of $1.70d \times 3.3d$ (the equivalent dimension of a pixel is 2.93 μm). Being MB^+ the only light-absorbing component among the

components involved in the reaction, the resulting intensity of the light across the specimen that is captured by the camera depends only on the MB^+ concentration. Light intensity images were converted into normalized depth averaged MB^+ concentration distribution by applying to each (ij)-th pixel the Lambert-Beer's law:

$$\frac{ln(I_{blank,ij}) - ln(I_{k,ij})}{ln(I_{blank,ij}) - ln(I_{max,ij})} = \frac{C_{k,ij}}{C_0} \tag{4}$$

where, $I_{k,ij}$ is the instantaneous value of the light intensity, $C_{k,ij}$ the MB^+ concentration, $I_{blank,ij}$ the light intensity acquired when the mixer is full of only the blank solution, and C_0 is the concentration when the mixer is full of the $C_0 = 5.3 \times 10^{-5}$ mol/L MB^+ solution. The reference values of $I_{blank,ij}$ and $I_{max,ij}$ are measured for each set of experiments, before using the two streams together. These references are evaluated as the arithmetic mean values over 80 frames each to reduce the effects of undesirable time-fluctuation of pixel intensity. Additional details on calibration, image post-processing, and experimental setup are provided in [27, 29, 30].

The optical rays in their course across the specimen are somewhat diverted due to refraction resulting from the slight differences in the refractive indexes of the two streams (viz. 1.33 for the MB^+ solution and 1.36–1.37 for the AsA solution [35]). Thus, darker or brighter streaks compared to the rest of the image were observed at the contact fronts of the two different solutions. The presence of these streaks in the acquired images was minimized by proper aperture adjustments of the condenser and the field diaphragms and focusing of the condenser. Streaks minimization was necessary to avoid offsetting the concentration measurement during the visualizations of the reaction progress.

On the contrary, streaks were deliberately highlighted and thus exploited to visualize the flow topology.

4. Numerical methodology and simulation set-up

Unsteady Navier-Stokes equations are solved along with the transport/reaction equations for all chemical species except water, i.e. MB^+, LMB^+, AsA, HCl and DA. The energy equation is not taken into account since thermal effects can be neglected. The non-dimensional form of the equations is:

$$\frac{\partial \hat{\rho}}{\partial \theta} + \nabla \cdot (\hat{\rho}\mathbf{u}) = 0, \tag{5}$$

$$\hat{\rho}\left(\frac{\partial \mathbf{u}}{\partial \theta} + \mathbf{u}\cdot\nabla\mathbf{u}\right) = -\nabla p + \frac{1}{Re}\nabla\cdot\left[\hat{\mu}\left(\nabla\mathbf{u} + \nabla\mathbf{u}^T\right)\right] + Ri\left(\hat{\rho}-1\right)\hat{\mathbf{g}}, \tag{6}$$

$$\hat{\rho}\left(\frac{\partial \phi_k}{\partial \theta} + \mathbf{u}\cdot\nabla\phi_k\right) = \frac{1}{Pe}\nabla\cdot\left(\hat{\rho}\hat{\mathcal{D}}_k\nabla\phi_k\right) + \frac{d\dot{\omega}_k}{\rho_0 U}, \tag{7}$$

where lengths are normalized with the mixing channel hydraulic diameter d and velocities with the inlet bulk velocity U. θ is the non-dimensional time, i.e. $\theta = \frac{tU}{d}$. In the above equations, $\mathbf{u}$ represents the non-dimensional velocity vector, p is the modified non-dimensional pressure, i.e. $p = (P - \rho_0 g Z)/\rho_0 U^2$, where P is the pressure, and g the gravity acceleration, while $\hat{\mathbf{g}}$ is the non-dimensional gravity, i.e. $\hat{\mathbf{g}} = \frac{\mathbf{g}}{g}$. $\hat{\rho} = \rho/\rho_0$ and $\hat{\mu} = \mu/\mu_0$ are non-dimensional density and viscosity, respectively, referred to a convenient reference state, i.e. μ_0 and ρ_0, which in our case corresponds to pure water at 20°C. Both density and viscosity are functions of the mixture composition as reported in [27]. ϕ_k represents the mass fraction of the k-th chemical species while $\dot{\omega}_k$

is its rate of production or consumption due to chemical reactions, which, for instance is $\dot{\omega}_{\mathrm{MB}^+} = -k_r \rho \phi_{\mathrm{MB}^+}$ for the methylene blue. $\hat{\mathcal{D}}_k = \mathcal{D}/\mathcal{D}_0$ is the non-dimensional diffusivity referred to the water self-diffusivity $\mathcal{D}_0$. The characteristic non-dimensional numbers are: the Reynolds number $Re = \frac{\rho_0 U d}{\mu_0}$, the Richardson number, $Ri = \frac{g d \Delta\rho}{\rho_0 U^2}$, and the Peclet number $Pe = \frac{U d}{\mathcal{D}_0}$, where $\Delta\rho$ is the density difference between the two inlet fluids. Both fluid density and viscosity depend on the ascorbic acid content ϕ_{AsA} and hence, the correlations $\mu = \mu_o f(\phi_{AsA})$ and $\rho = \rho_o g(\phi_{AsA})$ from [36] are implemented in the model, see for details [28, 29]. Despite stratification is negligible in the range of Re for which unsteady flows occur, we retained the full formulation of the governing equations, including the term related to gravity.

Uniform velocity and concentration of the reactants are imposed at the entrance of the inlet channels, whereas no-slip velocity at the channel walls and pressure outlet conditions at ambient pressure are set at the outlet boundary.

The transient solver of the finite volume code ANSYS Fluent v.19, was employed. Time advancement was handled with a second-order implicit method, by using a time step corresponding to a Courant–Friedrichs–Lewy number $CFL \cong 5$, while a second-order upwind interpolation scheme was used for spatial discretization. The PISO algorithm was employed for the pressure–velocity coupling. The computational grid is fully structured with 4.7 M cells; the cells are cubical at the confluence region, while they elongate along the inlet and the outlet channels. Such numerical setup has been successfully bench-marked against a massive parallel spectral element code in [37] where details on the grid independence study are also given.

5. Main flow features

5.1. Asymmetric periodic regime

The experimental flow visualizations (top) and the numerical isocontours of the vortex indicator λ_2 [38] (bottom) shown in Fig. 2 give an overview of the asymmetric unsteady flow regime taking place in the T-mixer at $Re = 320$ for [AsA]=0.85mol/L and for [AsA]=1.7mol/L. Six different instants within a temporal cycle are reported. These time instants are made non-dimensional with respect to the cycle period, i.e., $\tau = \frac{d}{USt}$ with St being the Strouhal number. For [AsA]=0.85mol/L (Figs. 2a-f) we estimated $St = 0.263$ from the numerical simulations, while the experimental value of the Strouhal number is $St = 0.268$, whereas for [AsA]=1.7mol/L (Figs. 2g-l) the simulations give $St = 0.253$ and the experiments $St = 0.246$, hence showing a very satisfactory agreement with each other.

Experimental flow visualizations and numerical vortical structures confirm the occurrence also for a reactive flow of the asymmetric unsteady regime, which has been described for non-reactive systems in [30]. A substantial agreement is found between the flow patterns obtained for the different AsA concentrations, and, thus, for the different reaction rates (compare Figs. 2a-f and Figs. 2g-l). In particular, at the T-junction the initial flow configuration (Fig. 2a and Fig. 2g at time $t/\tau = 0$) resembles the one of the engulfment regime, with the top part of the U-shaped vortical structures that are tilted. During the temporal evolution, the tilting angle increases while the vortical structures approach each other, merge and annihilate (Fig. 2b and Fig. 2h). Simultaneously, the co-rotating vortical structures in the mixing channel generate a blob of vorticity (see Fig. 2c and Fig. 2i), which is convected along

the mixing channel (Figs. 2d,e and Figs. 2j,k). For $0.45 \leq t/\tau \leq 1$, in the top part of the mixing channel the configuration typical of the steady engulfment regime, in which two counter-rotating vortical structures originate in the recirculation regions near the top walls of the mixer, is formed again.

A further insight on the flow patterns is obtained through the comparison between experimental and numerical instantaneous velocity fields and streamlines on the horizontal mid-plane of the mixing channel ($Z = 0.375$), shown in Fig. 3. We consider [AsA]=0.85mol/L and the same time instants as in Figs. 2a-f. The agreement between PIV experiments and numerical simulations is remarkable, with differences between the velocity fields always below a few percent (evaluated by using the L2 norm). The reproducibility of experimental results is estimated by evaluating the standard deviation in the velocity magnitude distributions obtained for the same valued of t/τ in different temporal cycles (see Fig. 4). The averaged values over $N = 25$ cycles of the standard deviation $\sigma(U)$ (evaluated by using the L2 norm) on the $Z = 0.375$ plane is always below $0.04U$, with maximum local values of approximately $0.11U$.

The same flow regimes are observed in the device when increasing Reynolds number, up to $Re = 460$ for [AsA]=0.85mol/L and $Re = 600$ for [AsA]=1.7mol/L. For the highest AsA concentration, instantaneous velocity fields and streamlines on the plane at $Z = 0.375$ are compared at $Re = 500$ in Fig. 5 to appreciate the agreement between experiments and simulations also at a higher Reynolds number. Again, six time instants are reported, made nondimensional by using the time period in the simulations, which corresponds to $St = 0.283$, and that of PIV data, corresponding to $St = 0.274$. The flow

pattern resembles the one previously described at $Re = 320$. The differences between experiments and simulations are slightly more pronounced than the ones at $Re = 320$, but still below 6% (evaluated by using the L2 norm).

5.2. Symmetric periodic regime

Similar experimental visualizations and λ_2 snapshots are shown in Figs. 6a-d for [AsA]=0.85mol/L at $Re = 500$ and in Figs. 6e-h for [AsA]=1.7mol/L at $Re = 650$. Four equispaced instants within a temporal cycle are reported, i.e. each $t/\tau = 0.25$. For the former value of [AsA], the numerical Strohual number is $St = 0.214$, while the experimental one is $St = 0.219$. For the latter one, numerical simulations indicated a $St = 0.228$, while the analysis of the experimental images leads to $St = 0.224$. Here we observe how at the confluence the flow preserves a large degree of symmetry, resembling the periodic unsteady regime described for water as the working fluid in [30]. The symmetric periodic regime occurs also in the present case involving a chemical reaction and fluids with different properties than water at $Re > 460$ for [AsA]=0.85mol/L and at $Re > 600$ for [AsA]=1.7mol/L. We notice from flow visualizations and λ_2-isosurfaces that the two streams are mainly segregated and just small oscillations occur in the contact region. Such segregation persists further down in the mixing channel. A remarkable agreement is found between experimental and numerical velocity fields also in this regime. As an example, the comparison is presented for [AsA]=0.85mol/L at $Re = 500$ in Fig. 7 for the mixer central plane. The same four time-instants as in Figs. 6a-d are considered. For both reaction rates, differences between the velocity fields are always below 4% (evaluated by using the L2 norm).

6. Mixing degree and reaction yield

We now investigate the effect of the dynamics and characteristics of the flow on the reaction. As in the previous section, the analysis is carried out first for the asymmetric periodic regime and then for the symmetric one.

6.1. Asymmetric periodic regime

First of all, we analyze the time behavior of the MB^+ reagent in the mixing channel. Figure 8 compares the experimental and numerical temporal signals of the MB^+ concentration averaged over three different cross-sections, viz. $y/d = -2$, $y/d = -7.5$ and $y/d = -25$ (from top to bottom) and made dimensionless with the incoming MB^+ concentration. Three combinations of Reynolds numbers and AsA concentrations within the periodic asymmetric regime are presented: $Re = 320$ and [AsA]= 0.85 mol/L in Fig. 8a, $Re = 320$ and [AsA]= 1.7 mol/L in Fig. 8b, and $Re = 500$ and [Asa]= 1.7 mol/L in in Fig. 8c. Four cycles are shown. The cycle is calculated as the product of the Strouhal number and the dimensionless time. It should be noted that the initial cycle time is arbitrary and does not correspond to those reported in the previous section. We can observe how the MB^+ signals clearly show a time-periodicity and the good agreement between experiments and numerical simulations confirms that the present experimental setup allows us to well capture the temporal evolution of the reaction.

The time-behavior of the MB^+ concentration resembles that of the passive scalar concentration for the same periodic regime in non-reactive systems [30]. The passage of the vorticity blob, described in Sec. 5.1, produces an increase in mixing and hence in the contact area between the two reagent

streams with a consequent positive effect on the consumption of MB^+ and thus on the progress of the reaction. If we examine in particular Fig. 8a, i.e. $Re = 320$ and [Asa]= 0.85 mol/L, we see that at $y/d = -2$, the signal exhibits a clear minimum in each cycle at $t/\tau = 0.7$, which is related to the passage of the vorticity blob. Moreover, an additional minimum is present at $t/\tau \approx 0$, corresponding to the instant when the vortical legs of the two co-rotating vortices in the mixing channel are stronger. On the other hand, a maximum in $C_{\mathrm{MB}^+}/C_{MB_0^+}$ is present in each cycle at $t/\tau = 0.85$, when the vorticity blob has moved downstream in the mixing channel and the co-rotating vortical structures start to form again. Moving downstream from the confluence area, i.e. $y/d = -7.5$ and $y/d = -25$, only the minimum linked to the passage of the blob remains evident in the signals. We can also observe how the MB^+ values decrease along the channel, as expected since the reaction proceeds; for $y/d = -25$ the non-dimensional average concentration of MB^+ fluctuates around 0.44.

Time signals for the reacting system with the fastest kinetics, i.e. [AsA]= 1.7 mol/L, are reported in Fig. 8b, for $Re = 320$, and in Fig. 8c, for $Re = 500$. The signals are qualitatively similar to those in Fig. 8a, but the amplitude of the fluctuations is larger than in the case of slower kinetics. As previously described, when the passage of the blob occurs in a cross-section, there is an increase in the degree of mixing which leads to an increase in MB^+ consumption. The faster the reaction is, the larger is the consumption of MB^+. This is evident by comparing Fig. 8b with Fig. 8a: at the same Re, the consumption of MB^+ is higher in the case with faster kinetics (Fig. 8b) and for the latter case the non-dimensional average concentration at $y/d = -25$

oscillates around 0.32 instead of 0.44. At $Re = 500$, the amplitude of the signal oscillations at $y/d = -2$ and $y/d = -7.5$ is somewhat higher than for $Re = 320$. Vortical structures become stronger by increasing Reynolds number (the same behavior holds in [30] considering water as the working fluid) and this has a positive effect on the contact area between the two reactant streams. Such positive effect counterbalances the negative effect that higher Re has on the residence time, i.e. its reduction with increasing the bulk velocity), ultimately leading to similar reaction progress. In fact, the normalized MB^+ concentration at $y/d = -25$ fluctuates around 0.345.

For the same three cases, Fig. 9 shows the instantaneous trends along the mixing channel of both the degree of mixing and the dimensionless average concentration of MB^+ obtained in the numerical simulations. Six time instants along a blob-shedding cycle are considered. As in [27, 37, 39], the degree of mixing is defined as $\delta_m = 1 - \frac{\sigma_b}{\sigma_{max}}$, where σ_b is the standard deviation of the volumetric passive tracer flow and σ_{max} is the maximum value of σ_b obtained for completely segregated streams. Thus, δ_m varies between $\delta_m = 0$, indicating a completely segregated flow, and $\delta_m = 1$, corresponding to a perfectly mixed flow. In the present work, the degree of mixing is computed by using the volumetric fraction of HCl, as this component does not participate in the chemical reaction and hence acts as a passive tracer. Consistently with the previous observations, a peak of the mixing degree curves corresponds to the passage of each vorticity blob (Figs. 9a,c,e), which contributes to increase the mixing of the reagents in the channel. The fingerprint of the flow dynamics is also evident in the trend along the mixing channel of the MB^+ concentration (Figs. 9b,d,f). For the case with a faster reaction, the fluctuations affect

the entire mixing channel (Figs. 9d,f), whereas in the case with the slower reaction the oscillations of the concentration of MB^+ are much smaller then those of δ_m. Clearly, in all cases, along the channel the concentration of MB^+ decreases as a result of the reaction.

6.2. Symmetric periodic regime

The same analyses as in the asymmetric regime are reported here for the symmetric periodic regime. Let us start from Fig. 10 that shows the time behaviors of the experimental and numerical normalized MB^+ concentration at different cross sections along the mixing channel at $Re = 500$ for [AsA]=0.85mol/L and at $Re = 650$ for [AsA]=1.7mol/L. As previously, we consider three cross-sections, viz. $y/d = -2$, $y/d = -7.5$, and $y/d = -25$. As described in Section 5.2, in the symmetric regime the flow unsteadiness mainly affects the interface between the two streams. The effects of the oscillation of the interface are clearly visible in the signals of MB^+ concentration in Fig. 10 and the agreement between experiments and simulations is excellent for both the reaction rates.

Also for the symmetric periodic regime, the numerical instantaneous signals in Fig. 11 of the mixing degree and of the normalized MB^+ concentration show the fingerprint of the dynamic behavior, which affects the entire mixing channel. Four signals in a cycle are considered. Oscillations in the instantaneous signals are again due the unsteadiness at the interface between the reactants. Comparing Fig. 11 and Fig. 8 between the symmetrical and asymmetrical regime, we can see a drastic reduction of the mixing degree in the symmetrical regime due to the segregation of the streams. Furthermore, the increase of the degree of mixing at the beginning of the outlet channel is not

sudden as in the case of the asymmetric regime. Indeed, in the asymmetric regime after 10 hydraulic diameters the mixing start to increase very slowly, while in the symmetrical regime this happens after a distance equal to 20 hydraulic diameters. Comparing Fig. 11a,b, i.e. $Re = 500$ and [AsA]= 0.85 mol/L, and Fig. 11c,d, i.e. $Re = 650$ and [AsA]= 1.7 mol/L, we see that the system with faster kinetics has signals with higher oscillations, especially for y/d up to -30. Moreover, it shows about 5% larger mixing degree towards the outlet of the channel, and achieves a higher consumption of MB^+.

6.3. Trends with Reynolds and Damköhler numbers

Experimental and numerical reaction yields are respectively reported in Fig. 12a and Fig. 12b as a function of the Reynolds number, along with data from the steady regimes already discussed in [28] (shown with white symbols). The reaction yield is evaluated at $y/d = -25$ as $\eta = 1 - 2\frac{C_{BM^+,Y=-25}}{C_{BM_0^+}}$, where $C_{BM^+,Y-25}$ is the MB^+ concentration averaged on the cross-section. The variation of the reaction yield along the cycle, evaluated in terms of standard deviation, is also shown. A good agreement is present between experiments and simulations. The role of flow regimes and kinetics on the reaction yield is highlighted in Fig. 12c and Fig. 12d, where experimental and numerical yields are shown as a function of the Damköhler number, describing the residence to chemical time-scale ratio, i.e. $Da = dk_{r,0}/U$. In the definition of Da, we chose the residence flow time, i.e. the time needed to the fluid flow to cover one hydraulic diameter and hence to cross the transversal mixer section, since we are treating flow regimes for which mixing is mainly promoted by the transverse convection induced by complex flow features, rather than diffusion. Moreover, this definition allows a direct comparison with the trends observed

for the steady regimes in [27]. The results show that the scaling, proposed in [27] for the vortex and engulfment regimes, holds also for the periodic asymmetric regime, as can be seen from the colored dashed lines in Fig. 12c and Fig. 12d. Indeed, in the periodic asymmetric regime:

$$\eta \propto \widetilde{k_{r,0}}^{0.5} Re^{0.4} \propto \frac{\widetilde{k_{r,0}}^{0.1}}{Da^{0.4}} \tag{8}$$

with $\widetilde{k_{r,0}} = k_{r,0}\frac{d^2}{\nu}$ being the non-dimensional kinetic constant that takes into account also fluid properties. Moreover, in [27] we showed that in the segregated regime, i.e. for large values of Da, the yield depends solely on Da as:

$$\eta \propto \frac{\widetilde{k_{r,0}}^{0.3}}{Re^{0.3}} \propto \widetilde{Da}^{0.3} \tag{9}$$

This behavior is confirmed here also for the periodic symmetric flow regime (shown in Fig. 12c,d with a solid gray line). Indeed, despite the presence of oscillations occurring in the contact region, flow segregation persists further down in the mixing channel in this regime, leading to a behavior analogous to the one of the steady segregated regime. For the lower reaction rate, the variance in time of the yield in this regime is small, as expected, and the value perfectly fits the trend of the steady segregated regime. Conversely, for the faster reaction rate, the time variance of η is large. This is due to the cross-section at which the yield is evaluated, i.e. $y/D = -25$. Indeed, from Fig. 11d it can be seen that in this region large oscillations in time and space are still present, which are reduced moving downstream. This may also explain the fact that the value of yield is slightly larger than the value predicted by the proposed fit (Figs. 12c,d). However, for consistency of the values and considerations previously published in the steady regimes [27, 28],

we prefer to consider $y/D = -25$ in all cases.

7. Conclusions

In the present work, experimental flow visualizations and velocity measurements of velocity and reactant concentration are used jointly with numerical simulations to investigate the mixing and reaction performance in the periodic flow regimes occurring in a T-shaped microreactor. We considered the effects of different kinetic constants, resulting in a wide range of Damköhler number which compares the scales of flow and chemistry.

As found in previous works for non-reactive systems, two different flow regimes are present for increasing the Reynolds number. The first is the periodic asymmetric regime, characterized by the presence in a part of the periodic cycle of a pattern resembling the one of the steady engulfment regime (two co-rotating vortical structures in the mixing channel), to which adds the shedding of vorticity-blobs along the mixing channel that forms from the collapse of the previously-mentioned vortical structures in the T-junction region. This leads to a further increase of the mixing performance compared to the engulfment regime. The second regime is the periodic asymmetric one, which is mainly a poor-mixed segregated regime with periodic oscillations at the interface between the two reactants.

Results show a remarkable agreement between experiments and simulations both in terms of flow pattern and reaction progress. For all cases, the unsteady flow dynamics leads to an unsteady behavior of mixing, and, hence, of the reaction yield, which are characterized by periodic time oscillations. In the unsteady asymmetric regime, in particular, the shedding of the vorticity blob

is found to give the largest contribution to mixing and reaction progress. However, the kinetic constant also plays a fundamental role, as expected, in the reaction progress; indeed, the reaction yield depends in both regimes on the Damköhler number. In the periodic asymmetric regime the reaction yield follows the same function of the Damköhler number and of a non-dimensional kinetic constant taking into account also fluid properties, previously proposed for the steady vortex and engulfment regimes. In the periodic symmetric regime, the reaction yield is found to depend only on the Damköhler number, with the same dependence previously highlighted for the steady segregated regime.

Acknowledgments

This work was supported by the University of Pisa - Italy through the "Progetti di Ricerca di Ateneo PRA 2017-2018" funding program. The authors are grateful to Sara Tomasi Masoni and Simone Egidi.

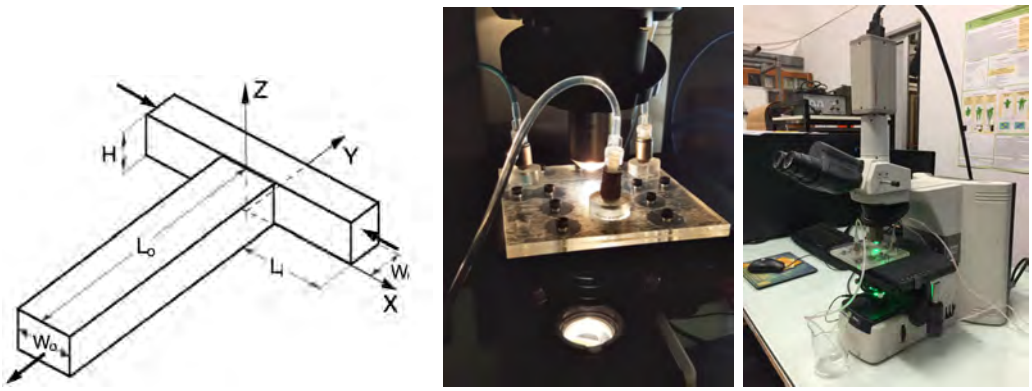

Figure 1: (a) Sketch of the T-reactor geometry and reference system, (b) picture of the T-reactor, (c) Particle Image Velocimetry set-up.

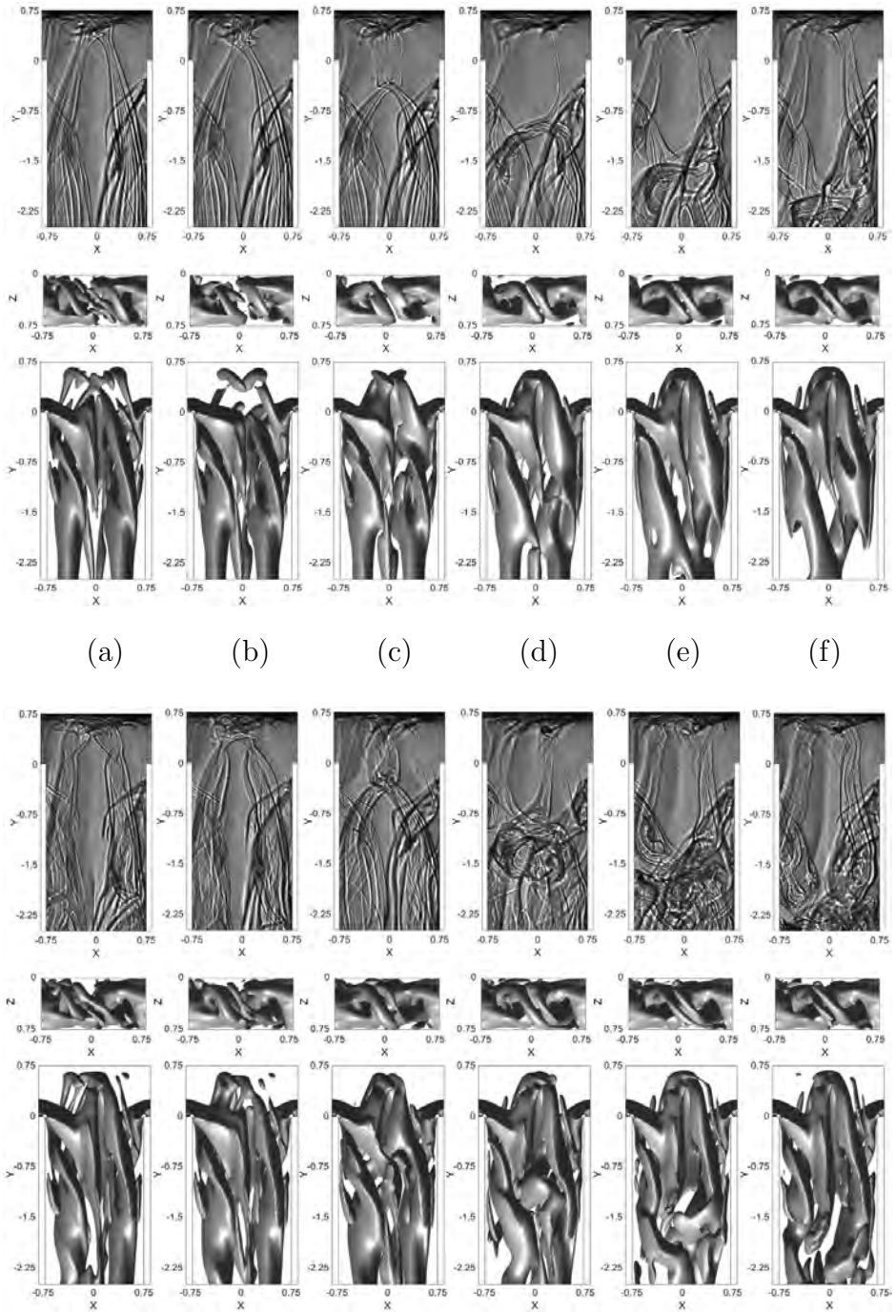

Figure 2: Experimental flow visualizations (top) and numerical isocontours of the vortex indicator λ_2 (bottom) at $Re = 320$ for [AsA]=0.85mol/L (a−f) and at $Re = 320$ for [AsA]=1.7mol/L (g−l). Considered times: (a,g) $t/\tau = 0$, (b,h) $t/\tau = 0.09$, (c,i) $t/\tau = 0.18$, (d,j) $t/\tau = 0.27$, (e,k) $t/\tau = 0.36$, (f,l) $t/\tau = 0.45$.

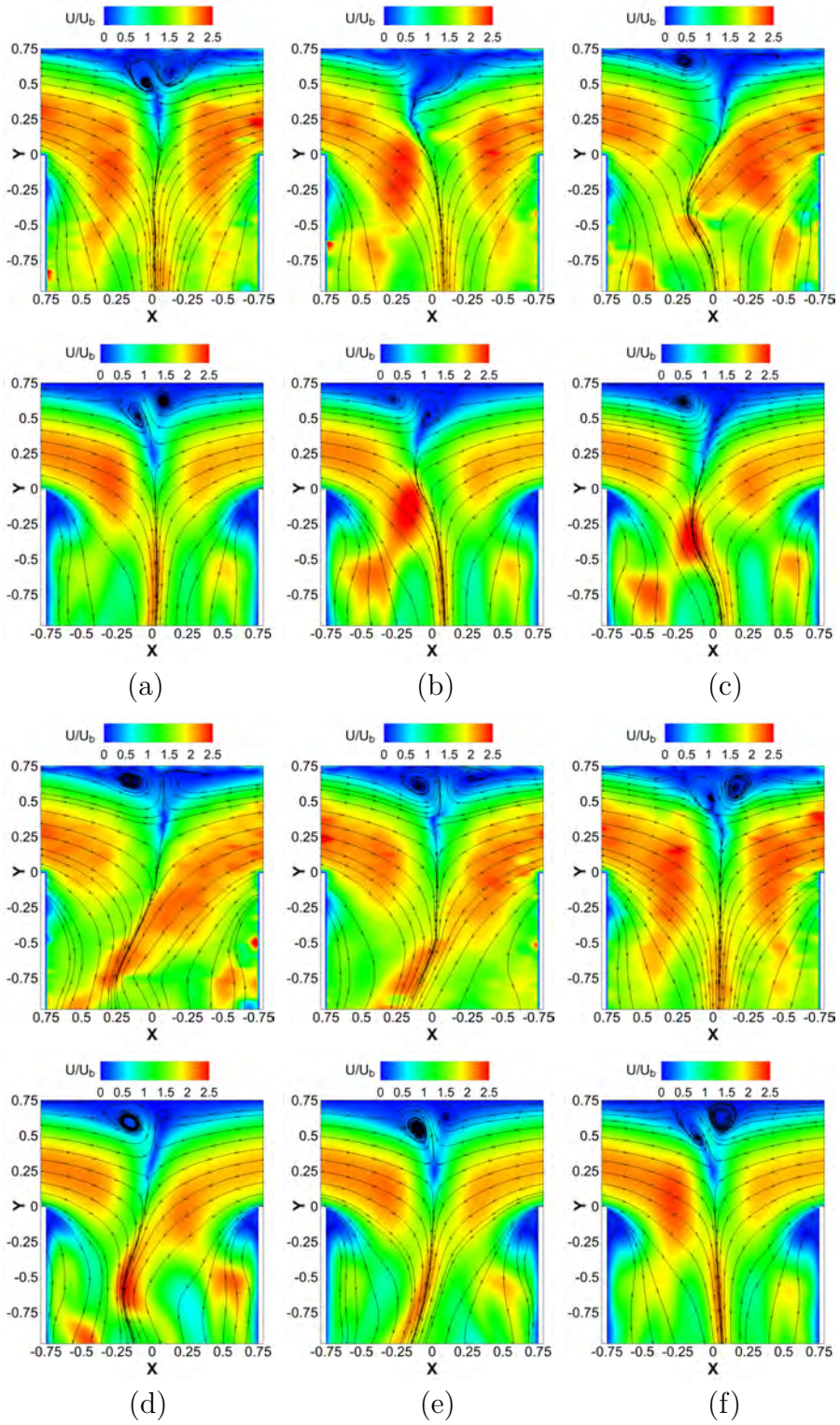

Figure 3: Experimental (top) and numerical (bottom) instantaneous velocity field and flow streamlines at $Re = 320$ for [AsA]=0.85mol/L. Considered times: (a) $t/\tau = 0$, (b) $t/\tau = 0.09$, (c) $t/\tau = 0.18$, (d) $t/\tau = 0.27$, (e) $t/\tau = 0.36$, (f) $t/\tau = 0.45$.

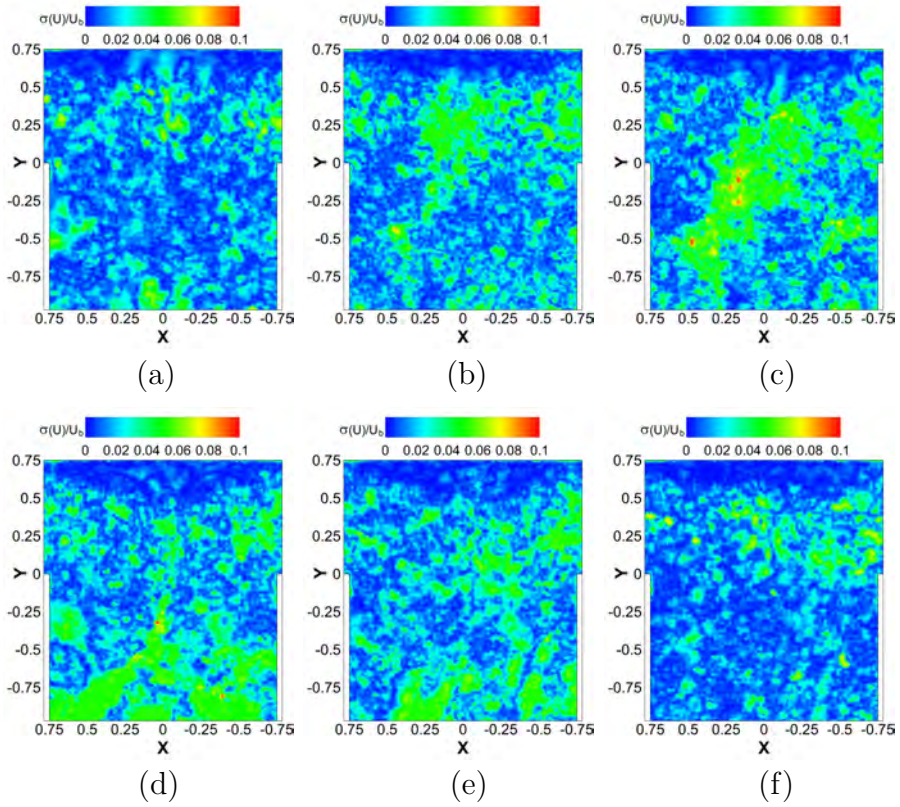

Figure 4: Standard deviation of the phase-averaged velocity field in the experiments at $Re = 320$ for [AsA]=0.85mol/L. Considered times: (a) $t/\tau = 0$, (b) $t/\tau = 0.09$, (c) $t/\tau = 0.18$, (d) $t/\tau = 0.27$, (e) $t/\tau = 0.36$, (f) $t/\tau = 0.45$.

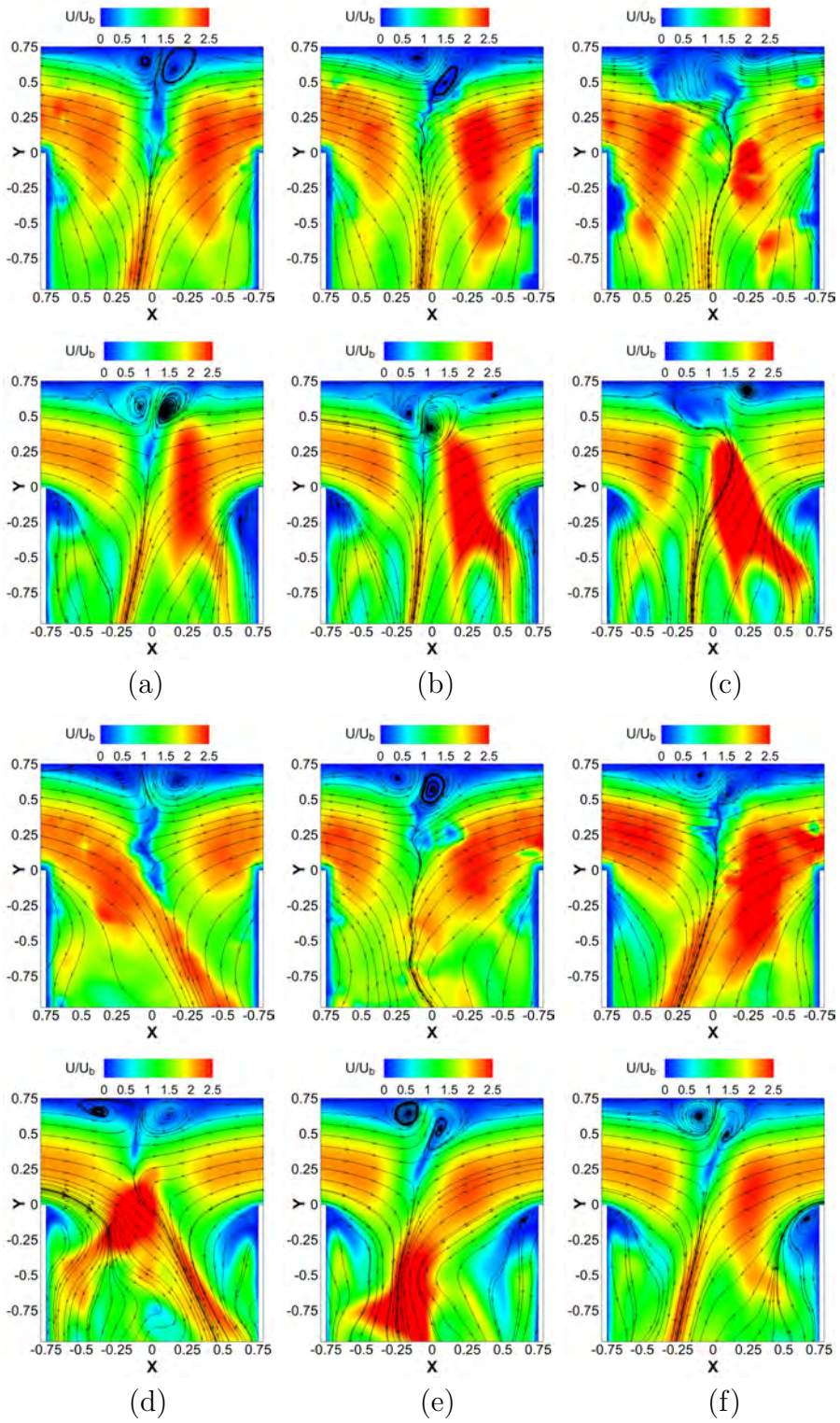

Figure 5: Experimental (top) and numerical (bottom) instantaneous velocity field and flow streamlines at $Re = 500$ for [AsA]=1.7mol/L. Considered times: (a) $t/\tau = 0$, (b) $t/\tau = 0.09$, (c) $t/\tau = 0.18$, (d) $t/\tau = 0.27$, (e) $t/\tau = 0.36$, (f) $t/\tau = 0.45$.

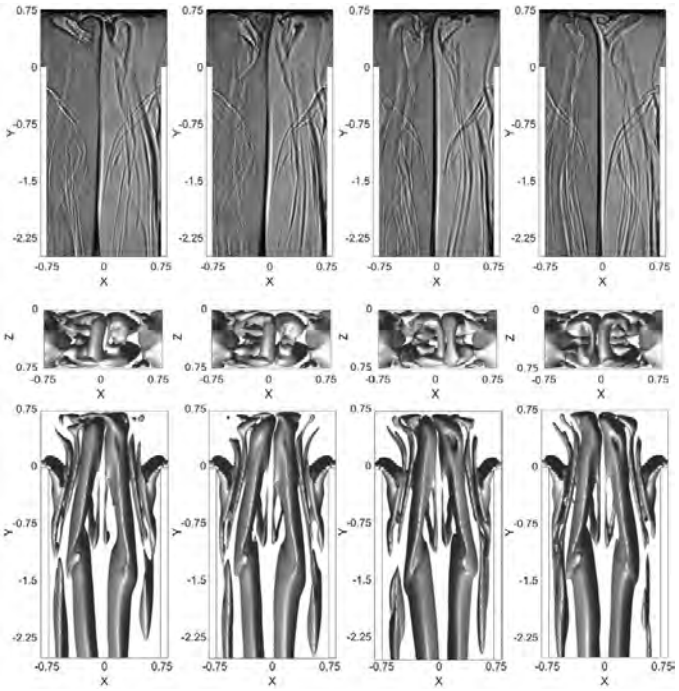

(a) (b) (c) (d)

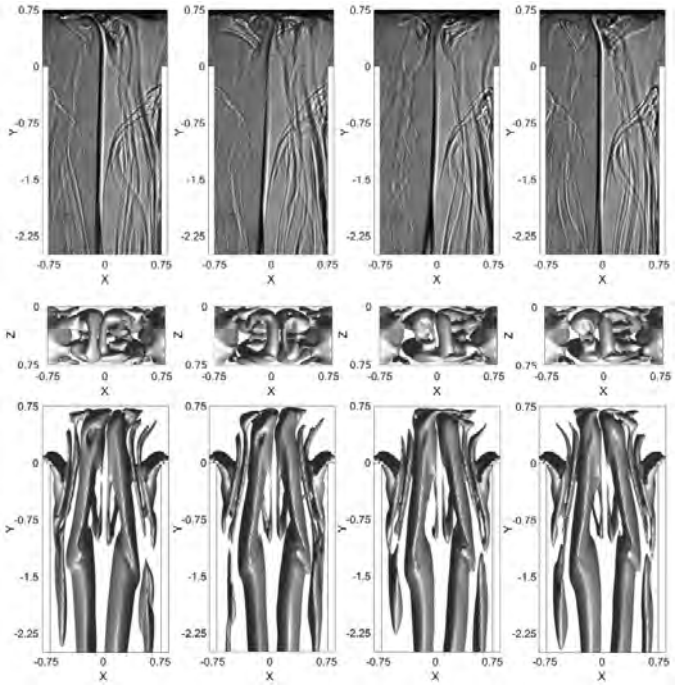

(e) (f) (g) (h)

Figure 6: Experimental flow visualizations (top) and numerical isocontours of the vortex indicator λ_2 (bottom) at $Re = 500$ for [AsA]=0.85mol/L (a−d) and at $Re = 650$ for [AsA]=1.7mol/L (e−h). Considered times: (a,e) $t/\tau = 0$, (b,f) $t/\tau = 0.25$, (c,g) $t/\tau = 0.50$, (d,h) $t/\tau = 0.75$.

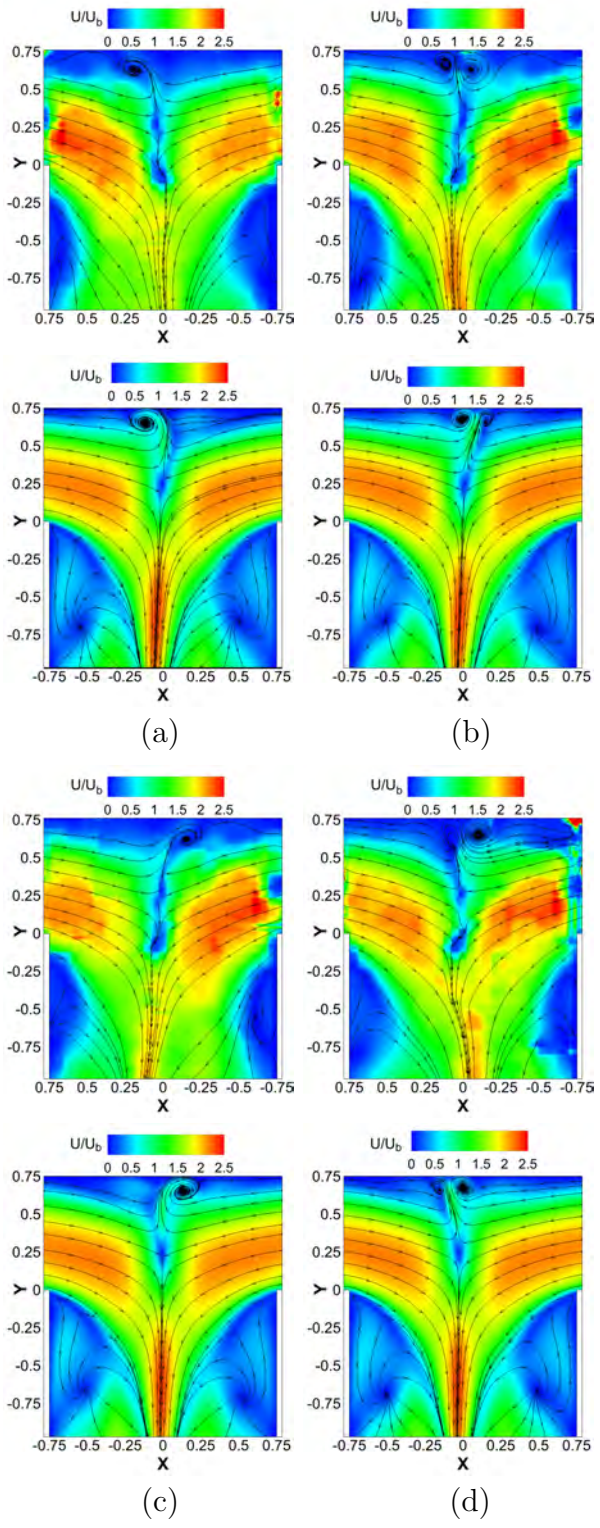

Figure 7: Experimental (top) and numerical (bottom) instantaneous velocity field and flow streamlines at $Re = 500$ for [AsA]=0.85mol/L. Considered times: (a) $t/\tau = 0$, (b) $t/\tau = 0.25$, (c) $t/\tau = 0.50$, (d) $t/\tau = 0.75$.

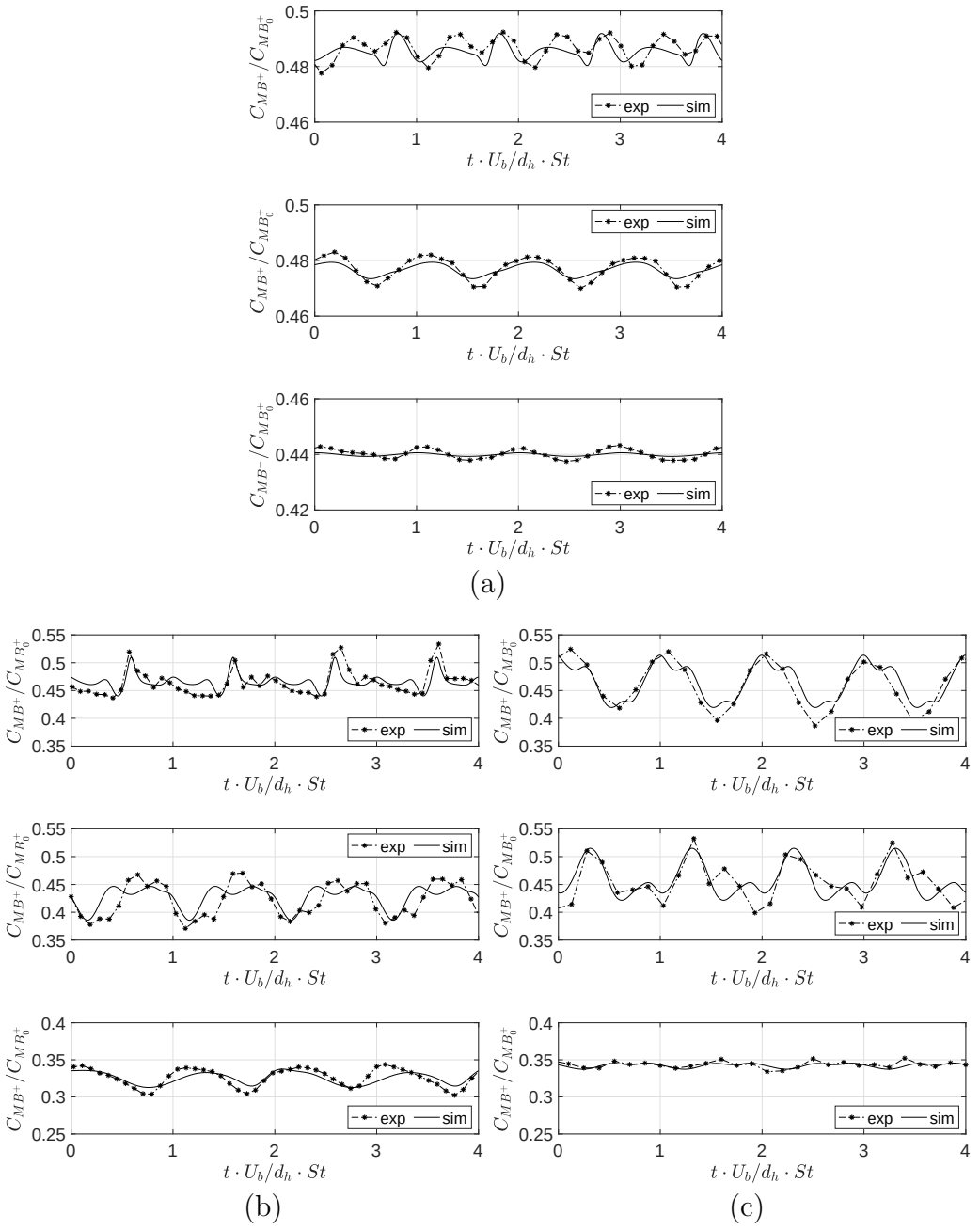

Figure 8: Time behavior of the experimental and numerical normalized MB^+ concentration along the mixing channel (a) at $Re = 320$ for [AsA]=0.85mol/L, (b) at $Re = 320$ for [AsA]=1.7mol/L, and (c) at $Re = 500$ for [AsA]=1.7mol/L. Considered cross sections (from top to bottom): $y/d = -2$, $y/d = -7.5$, and $y/d = -25$.

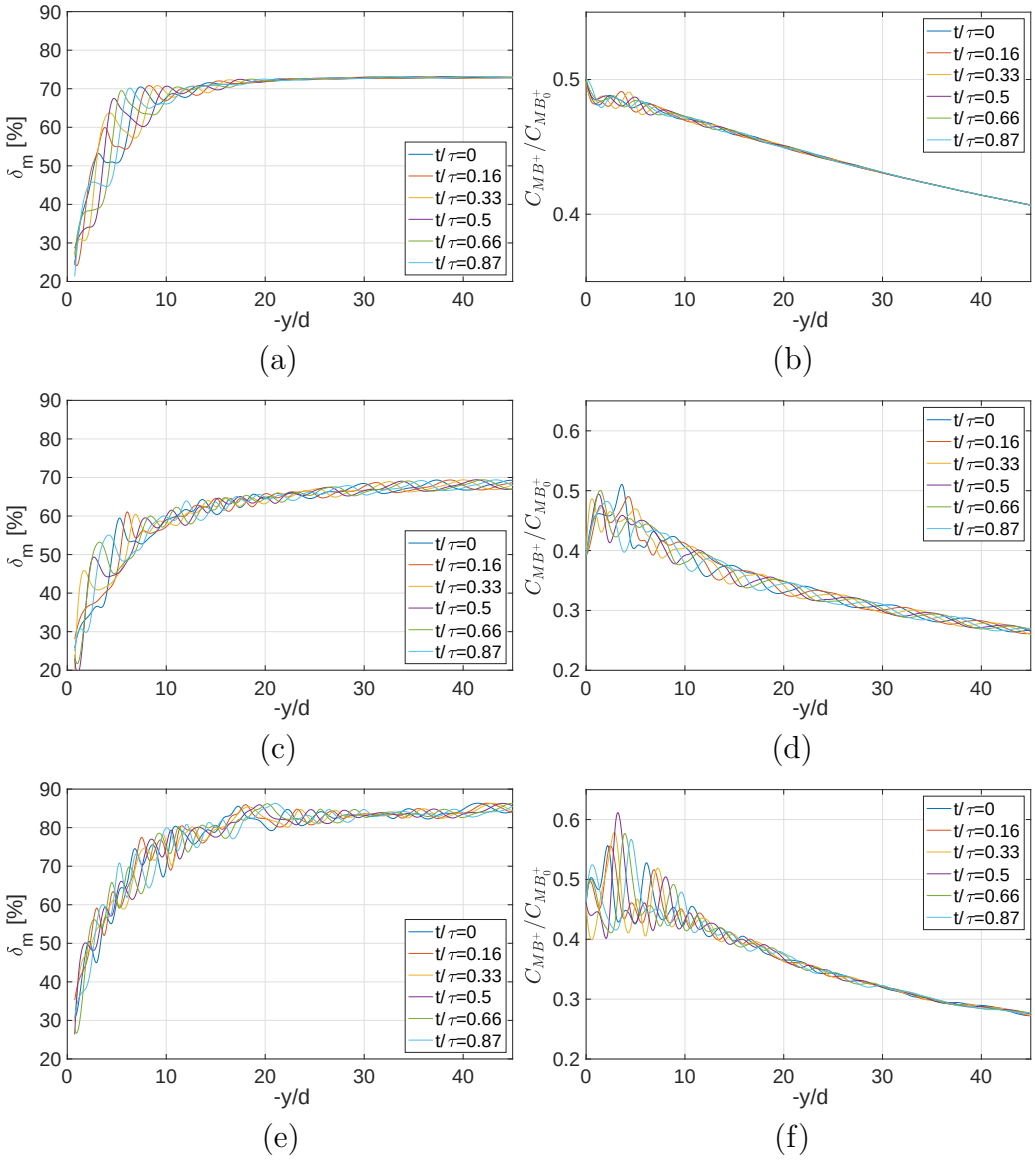

Figure 9: Instantaneous (a,c,e) mixing degree and (b,d,f) normalized MB^+ concentration along the mixing channel, evaluated from numerical simulations. Considered cases: (a,b) $Re = 320$ and [AsA]=0.85mol/L, (c,d) $Re = 320$ and [AsA]=1.7mol/L, and (e,f) $Re = 500$ and [AsA]=1.7mol/L.

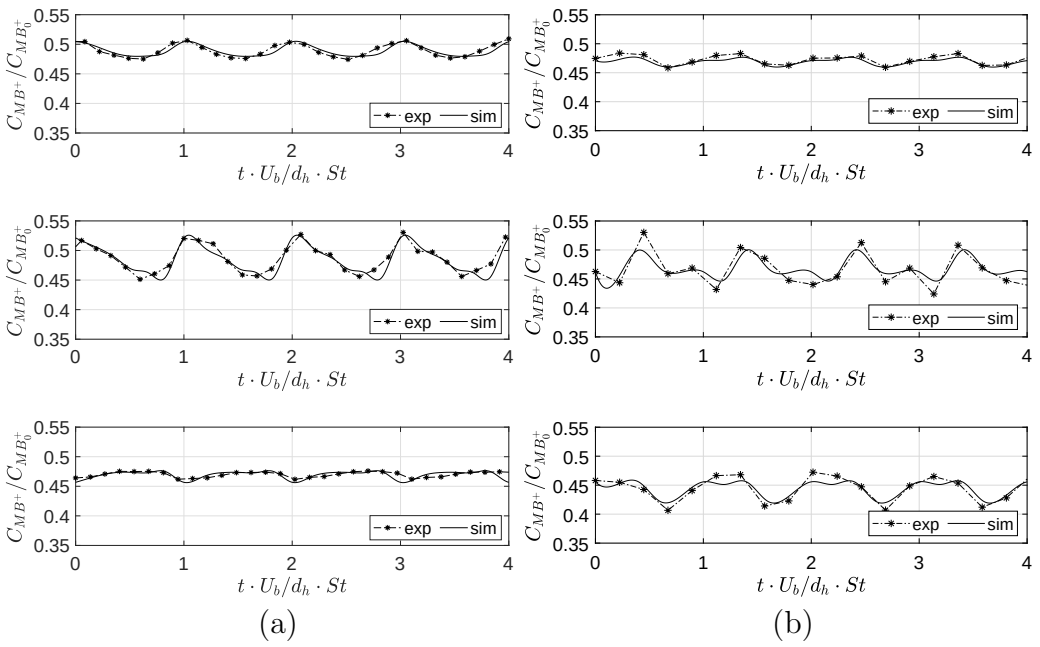

Figure 10: Time behavior of the experimental and numerical normalized MB^+ concentration along the mixing channel (a) at $Re = 500$ for [AsA]=0.85mol/L and (b) at $Re = 650$ for [AsA]=1.7mol/L. Considered cross sections (from top to bottom): $y/d = -2$, $y/d = -7.5$, and $y/d = -25$.

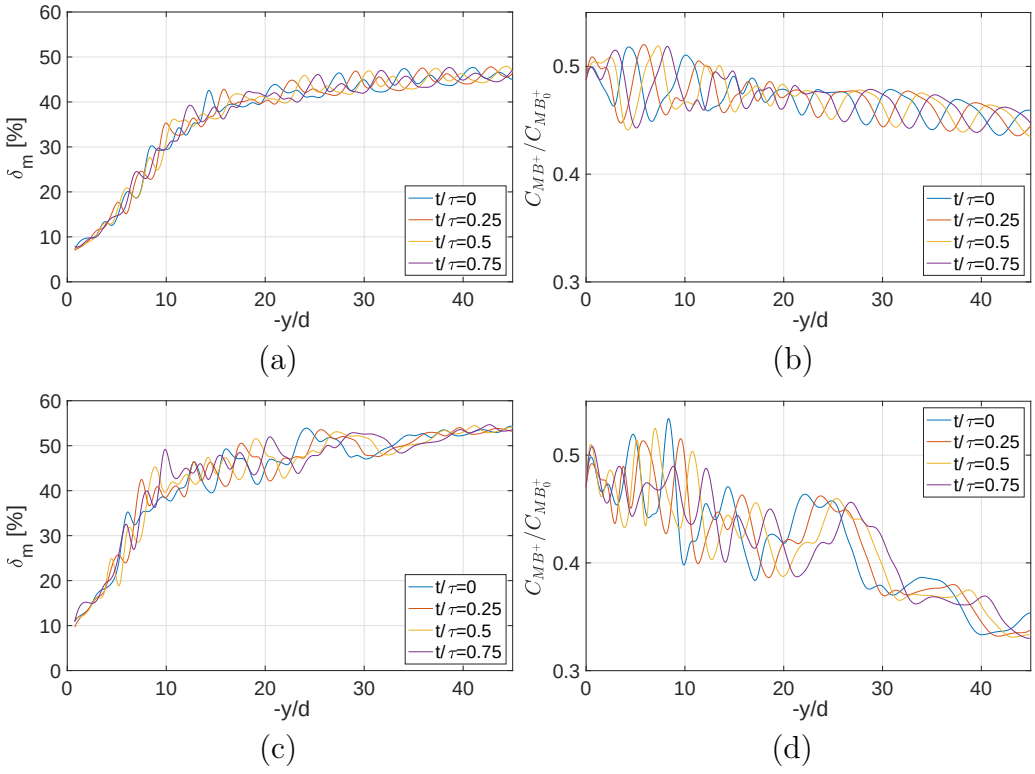

Figure 11: Instantaneous (a,c) mixing degree and (b,d) MB^+ concentration at different cross sections along the mixing channel, evaluated from numerical simulations. Considered cases: (a,b) $Re = 500$ and [AsA]=0.85mol/L, (c,d) $Re = 650$ and [AsA]=1.7mol/L.

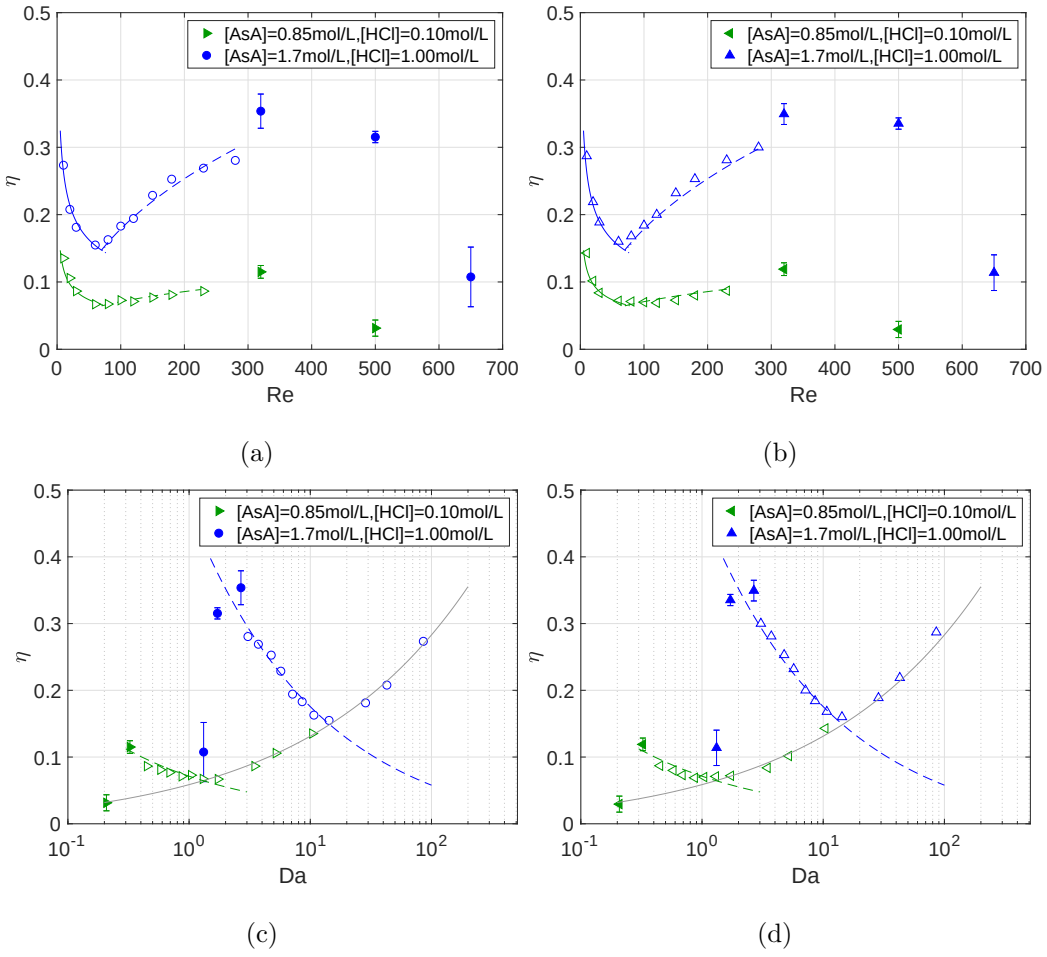

Figure 12: Reaction yield at $y/d = -25$ in (a,c) experiments and (b,d) numerical simulations: (a,b) η vs. Reynolds and (c,d) η vs. Damköhler.

List of Symbols

AsA	ascorbic acid
C	depth-averaged concentration, mol m^{-3}
C_{MB^+}	methylene blue concentration, mol m^{-3}
CFL	Courant–Friedrichs–Lewy number, -
d	mixing channel hydraulic diameter, m
$\mathcal{D}$	diffusivity, m^2 s^{-1}
$\mathcal{D}_0$	water self-diffusivity, m^2 s^{-1}
$\hat{\mathcal{D}}_k$	non-dimensional diffusivity, -
Da	Damköhler number, -
DA	dehydroascorbic acid
g	gravity acceleration, m s^{-2}
$\hat{\mathbf{g}}$	non-dimensional gravity, -
H	channel height, m
HCl	hydrogen chloride
I	light intensity, -
k_0	kinetic constant of the uncatalyzed test reaction, $mol^{-1}s^{-1}$
k_1	kinetic constant of the catalyzed test reaction, $L^2mol^{-2}s^{-1}$
k_r	kinetic constant of the pseudo-first-order test reaction, s^{-1}
$\widetilde{k_{r,0}}$	non-dimensional kinetic constant, -
L_i	inlet channel length, m
LMB^+	leucomethylene blue
L_o	mixing channel length, m
MB^+	methylene blue
N	number of cycles, -

$N.A.$	numeric aperture, -
p	modified non-dimensional pressure, -
P	pressure, Pa
Pe	Peclet number ($\frac{Ud}{\mathcal{D}_0}$), -
Re	Reynolds number ($\frac{\rho_0 U d}{\mu_0}$), -
Ri	Richardson number ($\frac{gd\,\Delta\rho}{\rho_0 U^2}$), -
St	Strouhal number ($\frac{d}{U\tau}$), -
t	time, s
δt	time interval of two subsequent pulses, s
Δt	image exposure time, s
U	bulk velocity, m s^{-1}
$\mathbf{u}$	non-dimensional velocity vector, -
W_i	inlet channels width, m
W_o	mixing channel width, m
x	x-coordinate, m
X	non-dimensional x-coordinate, -
y	y-coordinate, m
Y	non-dimensional y-coordinate, -
z	z-coordinate, m
Z	non-dimensional z-coordinate, -

Greek symbols

δ_m	degree of mixing, -
η	reaction yield, -
θ	non-dimensional time, -
μ	dynamic viscosity, kg m^{-1} s^{-1}
μ_0	dynamic viscosity of pure water at 20°C, kg m^{-1} s^{-1}
$\hat{\mu}$	non-dimensional dynamic viscosity, -
ν	kinematic viscosity, m^2 s^{-1}
ρ	density, kg m^{-3}
ρ_0	density of pure water at 20°C, kg m^{-3}
$\hat{\rho}$	non-dimensional density, -
σ	standard deviation, -
σ_b	standard deviation of the volumetric dye flow, -
σ_{max}	maximum value of the standard deviation of the volumetric dye flow, -
τ	cycle period, s
ϕ_k	mass fraction of the k-th chemical species,
$\dot{\omega}_k$	rate of production or consumption of ϕ_k due to chemical reactions, kg m^{-3} s^{-1}

References

[1] S. Lomel, L. Falk, J.M. Commenge, J.L. Houzelot, and K. Ramdani. The microreactor: A systematic and efficient tool for the transition from batch to continuous process? *Chem. Eng. Res. Des.*, 84(5 A):363–369, 2006.

[2] I. Rossetti and M. Compagnoni. Chemical reaction engineering, process design and scale-up issues at the frontier of synthesis: Flow chemistry. *Chem. Eng. J.*, 296:56, 2016.

[3] R. Gani, J. Bałdyga, B. Biscans, E. Brunazzi, J.-C. Charpentier, E. Drioli, H. Feise, A. Furlong, K. M. Van Geem, J.-C. de Hemptinne, A. J. B. ten Kate, G. M. Kontogeorgis, F. Manenti, G. B. Marin, S. S. Mansouri, P. M. Piccione, A. Povoa, M. A. Rodrigo, B. Sarup, E. Sorensen, I. A. Udugama, and J. M. Woodley. A multi-layered view of chemical and biochemical engineering. *Chem. Eng. Res. Des.*, 155:A133–A145, 2020.

[4] D. M. Roberge, L. Ducry, N. Bieler, P. Cretton, and B. Zimmermann. Microreactor technology: a revolution for the fine chemical and pharmaceutical industries? *Chem. Eng. Technol.*, 28:318, 2005.

[5] A. Pommella, G. Tomaiuolo, A. Chartoire, S. Caserta, G. Toscano, S. P. Nolan, and S. Guido. Palladium-N-heterocyclic carbene (NHC) catalyzed CaN bond formation in a continuous flow microreactor. effect of process parameters and comparison with batch operation. *Chem. Eng. J.*, 223(Supplement C):578, 2013.

[6] I. Rossetti. Continuous flow (micro-)reactors for heterogeneously catalyzed reactions: Main design and modelling issues. *Catal. Today*, 308:20–31, 2018.

[7] J. Antes, D. Boskovic, H. Krause, S. Loebbecke, N. Lutz, T. Tuercke, and W. Schweikert. Analysis and improvement of strong exothermic nitrations in microreactors. *Chem. Eng. Res. Des.*, 81(7):760–765, 2003.

[8] D. Russo, G. Tomaiuolo, R. Andreozzi, S. Guido, A.A. Lapkin, and I. Di Somma. Heterogeneous benzaldehyde nitration in batch and continuous flow microreactor. *Chem. Eng. J.*, 377:120346, 2019.

[9] Patrick Löb, Holger Löwe, and Volker Hessel. Fluorinations, chlorinations and brominations of organic compounds in micro reactors. *J. Fluorine Chem.*, 125(11):1677–1694, 2004.

[10] N. Kockmann, T. Kiefer, M. Engler, and P. Woias. Convective mixing and chemical reactions in microchannels with high flow rates. *Sens. Actuators B*, 117:495–508, 2006.

[11] N. Kockmann and D. M. Roberge. Transitional flow and related transport phenomena in curved microchannels. *Heat Transfer Eng.*, 32:595, 2011.

[12] S. Hossain and K.-Y. Kim. Mixing analysis in a three-dimensional serpentine split-and-recombine micromixer. *Chem. Eng. Res. Des.*, 100:95–103, 2015.

[13] V. Viktorov, M.R. Mahmud, and C. Visconte. Design and characterization of a new h-c passive micromixer up to reynolds number 100. *Chem. Eng. Res. Des.*, 108:152–163, 2016.

[14] M. Riccomi, F. Alberini, E. Brunazzi, and D. Vigolo. Ghost Particle Velocimetry as an alternative to PIV for micro/milli-fluidic devices. *Chem. Eng. Res. Des.*, 133:183, 2018.

[15] T. Dehghani, F. Sadegh Moghanlou, M. Vajdi, M. Shahedi Asl, M. Shokouhimehr, and M. Mohammadi. Mixing enhancement through a mi-

cromixer using topology optimization. *Chem. Eng. Res. Des.*, 161:187–196, 2020.

[16] M. Hoffmann, M. Schlüter, and N. Räbiger. Experimental investigation of liquid-liquid mixing in T-shaped micro-mixers using micro-LIF and micro-PIV. *Chem. Eng. Sci.*, 61:2968, 2006.

[17] J. Hussong, R. Lindken, M. Pourquie, and J. Westerweel. Numerical study on the flow physics of a t-shaped micro mixer. In Marco Ellero, Xiangyu Hu, Jochen Fröhlich, and Nikolaus Adams, editors, *IUTAM Symposium on Advances in Micro- and Nanofluidics*, pages 191–205, Dordrecht, 2009. Springer Netherlands.

[18] S. Thomas and T. Ameel. An experimental investigation of moderate reynolds number flow in a T-channel. *Exp. Fluids*, 49:1231, 2010.

[19] S. Thomas, T. Ameel, and J. Guilkey. Mixing kinematics of moderate reynolds number flows in a T-channel. *Phys. Fluids*, 22:006001, 2010.

[20] A. Mariotti, C. Galletti, R. Mauri, M. V. Salvetti, and E. Brunazzi. Steady and unsteady regimes in a T-shaped micro-mixer: Synergic experimental and numerical investigation. *Chem. Eng. J.*, 341:414, 2018.

[21] S. Camarri, A. Mariotti, C. Galletti, E. Brunazzi, R. Mauri, and M.V. Salvetti. An Overview of Flow Features and Mixing in Micro T and Arrow Mixers. *Ind. Eng. Chem. Res.*, 59(9):3669–3686, 2020.

[22] M. Engler, N. Kockmann, T. Kiefer, and P. Woias. Numerical and experimental investigations on liquid mixing in static micromixers. *Chem. Eng. J.*, 101:315–322, 2004.

[23] S. Dreher, N. Kockmann, and P. Woias. Characterization of laminar transient flow regimes and mixing in T-shaped micromixers. *Heat Transfer Eng.*, 30:91, 2009.

[24] A. Mariotti, C. Galletti, E. Brunazzi, and M. V. Salvetti. Steady flow regimes and mixing performance in arrow-shaped micro-mixers. *Phys. Rev. Fluids*, 4:034201, 2019.

[25] C. Galletti, E. Brunazzi, and R. Mauri. Unsteady mixing of binary liquid mixtures with composition-dependent viscosity. *Chem. Eng. Sci.*, 164:333–343, 2019.

[26] A.S. Lobasov and A.V. Minakov. Analyzing mixing quality in a t-shaped micromixer for different fluids properties through numerical simulation. *Chem. Eng. Process.*, 124:11–23, 2018.

[27] A. Mariotti, M. Antognoli, C. Galletti, R. Mauri, M. V. Salvetti, and E. Brunazzi. The role of flow features and chemical kinetics on the reaction yield in a t-shaped micro-reactor. *Chem. Eng. J.*, 396:125223, 2020.

[28] A. Mariotti, C. Galletti, R. Mauri, M.V. Salvetti, and E. Brunazzi. Effect of stratification on the mixing and reaction yield in a T-shaped micro-mixer. *Phys. Rev. Fluids*, 004200:1–29, 2021.

[29] A. Mariotti, M. Antognoli, C. Galletti, R. Mauri, M.V. Salvetti, and E. Brunazzi. A study on the effect of flow unsteadiness on the yield of a chemical reaction in a T micro-reactor. *Micromachines*, 12:242, 2021.

[30] A. Mariotti, C. Galletti, M. V. Salvetti, and E. Brunazzi. Unsteady flow regimes in a T-shaped micromixer: Mixing and characteristic frequencies. *Ind. Eng. Chem. Res.*, 58(29):13340–13356, 2019.

[31] S. Mowry and P. J. Ogren. Kinetics of methylene blue reduction by ascorbic acid. *J. Chem. Educ.*, 76:970–973, 1999.

[32] R. Lindken, J. Westerweel, and B. Wieneke. Stereoscopic micro particle image velocimetry. *Exp. Fluids*, 41:161, 2006.

[33] R. Lindken, M. Rossi, S. Große, and J. Westerweel. Micro-particle image velocimetry (PIV): Recent developments, applications, and guidelines. *Lab on a Chip - Miniaturisation for Chemistry and Biology*, 9:2551, 2009.

[34] M. G. Olsen and R. J. Adrian. Out-of-focus effects on particle image visibility and correlation in microscopic particle image velocimetry. *Exp. Fluids*, 29:166–174, 2000.

[35] M. Shamim and S. Khoo. Some physical properties of aqueous L-ascorbic acid solutions. *Aust. J. Chem.*, 32:2293–2295, 1979.

[36] E. Nishikata, T. Ishii, and T. Ohta. Viscosities of aqueous hydrochloric acid solutions, and densities and viscosities of aqueous hydroiodic acid solutions. *J. Chem. Eng. Data*, 26:254–256, 1981.

[37] C. Galletti, A. Mariotti, L. Siconolfi, R. Mauri, and E. Brunazzi. Numerical investigation of flow regimes in T-shaped micromixers: benchmark between finite volume and spectral element methods. *Can. J. Chem. Eng.*, 97:528–541, 2019.

[38] J. Jeong and F. Hussain. On the identification of a vortex. *J. Fluid Mech.*, 285:69–94, 1995.

[39] C. Galletti, G. Arcolini, E. Brunazzi, and R. Mauri. Mixing of binary fluids with composition-dependent viscosity in a T-shaped micro-device. *Chem. Eng. Sci.*, 123:300, 2015.